1 *Article*

2 # Synthetic packed-bed generation for CFD
3 # simulations: Blender vs. STAR-CCM+

4 **Steffen Flaischlen[1,2]*, Gregor D. Wehinger[1,2†]**

5 [1] Institute of Chemical and Electrochemical Process Engineering, Clausthal University of Technology,
6   Leibnizstr. 17, 38678 Clausthal-Zellerfeld, Germany
7 [2] Research Center Energy Storage Technologies (EST), Clausthal University of Technology, Am Stollen 19A,
8   38640 Goslar, Germany

9 * Correspondence: flaischlen@icvt.tu-clausthal.de, Tel.: 0049 05323-72-2561

10 † Email address: wehinger@icvt.tu-clausthal.de

11

12 **Abstract:** A common reactor type in the chemical and process industry is the fixed-bed reactor.
13 Accurate modeling can be achieved with particle-resolved Computational Fluid Dynamic (CFD)
14 simulations. However, the underlying bed morphology plays a paramount role. Synthetic bed-
15 generation methods are much more flexible and faster than image-based approaches. In this study,
16 we look critically at the two different bed generation methods: Discrete Element Method (DEM) (in
17 the commercial software STAR-CCM+) and the rigid-body model (in the open-source software
18 Blender). The two approaches are compared in terms of synthetically generated beds with
19 experimental data of overall and radial porosity, particle orientation, as well as radial velocities.
20 Both models show accurate agreement for the porosity. However, only Blender shows similar
21 particle orientation than the experimental results. The main drawback of the DEM is the long
22 calculation time and the shape approximation with composite particles.
23
24
25 **Keyword**s: Fixed-bed reactor, Blender, Discrete Element Method, CFD
26

27 **1. Introduction**

28   Fixed-bed reactors are frequently used in the chemical and process industry, e.g. in
29 heterogeneous catalysis, where the products are separated from the catalyst. Such catalytic fixed-bed
30 reactors can be described with conventional engineering models on several levels of detail ranging
31 from pseudo-homogeneous one-dimensional models to heterogeneous two-dimensional models [1,
32 2]. For reactor arrangements with a low tube-to-particle diameter ratio $\left(\frac{D}{d_\mathrm{p}} = N < 10\right)$, the effect of
33 the confining walls have a large impact on the flow field and hence on the pressure drop [3, 4], radial
34 heat transfer [5] and consequently on the reaction rates. Over the last two decades, experiments of
35 small *N* packed beds were accompanied with particle-resolved Computational Fluid Dynamic (CFD)
36 simulations in order to investigate the local interactions of transport phenomena, also in combination
37 with local reaction kinetics [6, 7].

38   In these particle-resolved CFD simulations, the fixed-bed morphology have to be as realistic as
39 possible, which leads to additional challenges. Image-based methods provide more or less direct
40 information of the bed morphology. For example, Wang et al. [8] conducted gamma-ray experiments
41 to receive statistical information about a fixed bed consisting of Pall rings and evaluated them with a
42 reconstruction algorithm. In another study, magnetic resonance imaging (MRI) was utilized to
43 generate three-dimensional geometries for CFD simulations [9]. Similar to a two-dimensional image
44 consisting of pixels, these images consist of three-dimensional voxels, which have to be converted

into a surface description of the particle bed. The downside of a real image of a packed bed is the high expenditure of time and the special equipment required for scanning. In addition, the transition between the solid particles and the free space is mapped without a clear boundary, requiring an algorithm to precisely define the boundaries of the particle [10]. One possibility to create a random structure is the *Monte Carlo Method*, where particles are randomly arranged in a container [11–13]. If a certain stability criterion is met, the particle is kept at this position, otherwise it is deleted. This process is repeated until a certain fixed-bed height is reached. Whereas the bed porosity is satisfactorily reproduced by Monte Carlo algorithms, Caulkin et al. [14, 15] showed that the local particle orientation was not in acceptable agreement with corresponding experiments.

The most widely used numerical method to generate synthetically packed-bed structures is the Discrete Element Method (DEM), based on the original work of Cundall and Strack [16]. In the DEM, the particles are filled into a container and the Newton's equation of motion are solved for the spherical particles. In the model, restitution and friction are taken into account. Furthermore, the contact forces between the particles (and between particles and the wall) are considered. The DEM has advantages over the Monte Carlo method, as it describes the physical process of filling more accurately. Wehinger and Kraume [17] showed satisfactory agreement of radial porosity profiles between packed beds of spheres and cylinders generated with DEM in comparison with experimental data. One disadvantage of the DEM is the very high computing effort, since the contact forces for each generated particle must be determined. In addition, the contact forces are modeled on the basis of a sphere, so that the representation of non-spherical pellets results in composite pellet [18, 19]. Kodam et al. [20, 21] developed a sophisticated contact-detection algorithm for cylindrical particles. Based on different contact scenarios, the authors proposed equations to calculate the overlap, location, and normal vector of the contacts between two cylindrical particles and between the particle and the wall. More recently, this approach was generalized and included into a more comprehensive workflow [22].

Rigid body simulations, such as joints, motors, collisions and contacts with friction, are very common in computer games, animation software and film production. Consequently over the last two decades, powerful software tools have been developed to capture such actions as realistic as possible [23]. One of them is Blender, an open source software, which has a physical library, Bullet Physics Library, included [24]. Recently, several research groups have been working on the possibility of using Blender for synthetic fixed-bed generation, see [25–29].

Boccardo et al. [25] firstly mentioned the application of Blender to generate packed beds of different particle shapes. This possibility of the very fast and computationally efficient computer graphics code to simulate complex particles represents the main advantage of Blender, while the generated packings showed a realistic description. Later, Boccardo et al. [26] presented an open-source workflow for the CFD simulation of packed bed reactors, where spheres, cylindrical beads, and trilobes were tested. Partopour and Dixon [27] validated bed structures of different pellet shapes generated with Blender with correlations from literature and experimental data from Giese et al. [30]. In addition, the authors compared the particle alignment of cylinders with experimental data from Caulkin et al. [15]. They found a general agreement between simulations and experiments. However, modeling details of the bed generation process and simulations times were not presented. Because of the easy accessible and in Blender included Python scripting, the authors presented an own automation script for packed-bed generation. Fernengel et al. [28] also used a Python script for a workflow of CFD simulations for packed-bed reactors in OpenFOAM. Finally Pavlišič et al. [29] applied Blender for beds of spherical and arbitrary particles (cylinders, trilobes and quadrilobes) and investigated with CFD simulations the pressure drop in packed beds. All these publications show that Blender is an easy-to-use open source tool for the synthetic generation of fixed beds with a high degree of automation.

93 Many authors claim that Blender is a computational efficient tool to generate packed beds. So
94 far, no comparison of different generation times have been shown. In addition, many studies compare
95 the synthetically generated beds only with experimental data and not with alternative approaches.
96 In this study, two approaches are applied to generate packings, of different particle shapes, i.e. the
97 rigid body approach represented by Blender and the commonly used soft body DEM represented by
98 STAR-CCM+ from Siemens PLM to generate packed beds made of different particle shapes [31]. The
99 comparison between the two approaches involves accuracy with experimentally derived mean
100 porosity values, radial porosity profiles, particle-orientation distribution, generation time, as well as
101 CFD simulations based on the generated beds in terms of local velocity profiles. After a closer look
102 at the methods, the results are presented and discussed, and finally a conclusion with modeling
103 recommendations are given.

104 **2. Methods**

105 *2.1 Packing Generation*

106 In this study, the Discrete Element Method (DEM) is applied in the framework of the CAE
107 software STAR-CCM+ from Siemens PLM [31]. DEM is a *Soft Body Approach* that takes into account
108 the deformation of bodies under the influence of acting forces [16]. In Blender, on the contrary, the
109 objects are assumed rigid and not deformable (*Rigid Body Approach*) [32]. This simplification is
110 justified for most catalyst carriers, since they consist of ceramic materials, which do not show any
111 deformations under acting forces. They are characterized by a high shear modulus, i.e. the
112 relationship between shear stress and shear strain. Typical shear modulus for ceramics are in the
113 order of 150 GPa, whereas deformable materials such as rubber show values in the order of 0.2 GPa
114 [33, 34]. In the following, the applied methods for both approaches are presented and the possibility
115 of adjustments will be discussed in more detail.

116 2.1.1 Discrete Element Method – Soft Body Approach in STAR-CCM+

117 The Discrete Element Method is a soft body approach based on the original work Cundall and
118 Strack [16]. It considers particles, in the original work spheres, as deformable bodies. Interactions
119 between the objects are calculated with the momentum balance equation (Newton´s second law).

$$m_p \cdot \frac{d\mathbf{v}_p}{dt} = \mathbf{F}_s + \mathbf{F}_b \tag{1}$$

120 Where m_p and $\mathbf{v_p}$ are the particle mass and velocity while t is the time. Forces that are acting on
121 the particle surface are described as surface forces $\mathbf{F}_s$ and $\mathbf{F}_b$ is the body force consisting of the
122 gravity force $\mathbf{F}_g$ and the contact forces $\mathbf{F}_c$.

$$\mathbf{F}_b = \mathbf{F}_g + \mathbf{F}_c \tag{2}$$

$$\mathbf{F}_c = \sum_{\text{neighbor particles}} \mathbf{F}_{\text{contact}} + \sum_{\text{neighbor walls}} \mathbf{F}_{\text{contact}} \tag{3}$$

123 The contact forces between the objects are calculated using a spring-dashpot system. With its
124 repulsive forces, the spring ensures that the particles are pushed apart representing the elastic part
125 of a collision. The dashpot, on the other hand, represents the energy dissipation by reducing the
126 collision forces simulating inelastic impacts. The forces are distributed in different directions. The
127 normal force F_n is represented by a parallel spring-dashpot system, while the force F_t in tangential
128 direction to the contact surface is represented by a parallel spring-dashpot system connected in series
129 with a slider. The contact force between two spheres is calculated according to (4) as the sum of the
130 normal and tangential forces magnitudes and the unit normal vectors $\mathbf{n}$ and $\mathbf{t}$.

$$\mathbf{F}_{\text{contact}} = F_n \cdot \mathbf{n} + F_t \cdot \mathbf{t} \tag{4}$$

131   In this soft body approach, the deformation of the particles under acting forces is characterized by
132   allowing overlaps between each other. STAR-CCM+ offers various models for the calculation of these
133   individual forces: Hertz-Mindlin no-slip contact model, linear spring contact model, and Walton
134   Braun hysteretic contact model. The simplest model is the Linear Spring model, which assumes a
135   linear relationship between the contact force and overlaps. A comparison of different models can be
136   found elsewhere [35]. The description of the contact force in normal direction is given by a term for
137   the spring and the dashpot. It depends on the normal spring stiffness K_n, the damping N_n , the
138   overlaps in normal direction d_n and the velocity at the contact point v_n.

$$F_n = -K_n \cdot d_n - N_n \cdot v_n \tag{5}$$

139   Therefore the normal spring stiffness is calculated with the equivalent Radius R_{eq} of the contacting
140   spheres, the maximum overlap δ_{max} and the equivalent Young's modulus E_{eq}:

$$K_n = \frac{4}{3} \cdot \sqrt{\frac{\delta_{max}}{R_{eq}}} \cdot E_{eq} \cdot R_{eq} \tag{6}$$

141   In order to determine damping, the damping coefficient N_{N-damp} is required, which is only
142   dependent on the set coefficient of restitution e_N:

$$N_{N-damp} = \frac{-\ln(e_N)}{\sqrt{\pi^2 + \ln(e_N)^2}} \tag{7}$$

143   With this damping coefficient, as well as the normal spring stiffness K_N and the equivalent particle
144   mass M_{eq}, the damping of the system in normal direction can be calculated:

$$N_N = 2 \cdot N_{N-damp} \cdot \sqrt{K_N \cdot M_{eq}} \tag{8}$$

145   The equations shown for the normal direction are also formulated equivalently for the tangential
146   direction. As a special feature, therefore, only the contact force in tangential direction F_t should be
147   considered, since this depends on the condition shown in (9).

$$|K_t \cdot d_t| < |K_t \cdot d_t| \cdot \mu \tag{9}$$

148   The additional material property is the static friction coefficient μ, which is an important factor in
149   fixed-bed filling processes. If the condition in (9) is fulfilled, (10) applies, otherwise (11) applies.

$$F_t = -K_t \cdot d_t - N_t \cdot v_t \tag{10}$$

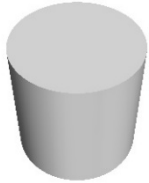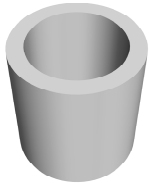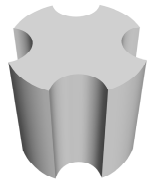$$F_t = \frac{|K_n \cdot d_n| \cdot \mu \cdot d_t}{|d_t|} \tag{11}$$
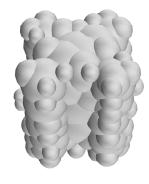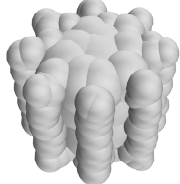
150   For further information on the equations and other contact force models, please refer to the STAR-
151   CCM+ manual and relevant DEM literature, e.g. Di Renzo and Di Maio [35], Zhu et al. [36]. In the
152   equations above, the material property values are:
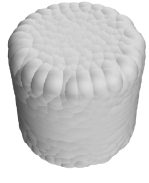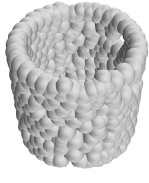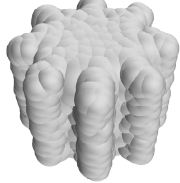153   • Density (used for calculation of the equivalent particle mass (8)
154   • Young´s modulus E (6)
155   • Poisson ratio (calculation of equivalent Young´s modulus) (6)
156   • Coefficient of restitution e (7)
157   • Static friction factor μ (9)((11)
158   The contact forces are calculated on the basis of a sphere. However, this consideration becomes
159   challenging, for non-spherical particles. The most frequently used method is the use of composite
160   particles. Complex particles are approximates with a user-defined number of spheres. These are
161   merged together in such a way that the shape of the composite particle approaches the original
162   particle shape. The outer surface of the spheres is used for contact detection and force modelling [18].
163   With a higher number of spheres, the accuracy of particle description is increasing. It has to be
164   considered that a representation with few spheres allows faster simulations, but due to the inaccurate
165   representation of the particles with no sharp edges, the resulting solution might deviate largely. For

166 further information please refer to Marigo and Stitt [19], where the effects of different shape
167 approximations are investigated for two configurations for a rotating drum. As examples, in Table 1
168 the composite particle description for different particles and different accuracy are shown.

169   **Table 1.** Different particle geometries and composite particle approximation.

CAD-Geometry				
Composite particle of 100 spheres				
Composite maximum				
	560 spheres	449 spheres	543 spheres	441 spheres

170
171   Remember that a higher number of spheres leads to a more exact approximation (e.g. sharper
172 edges), but also to higher simulation times. Therefore, the choice of the number of spheres represents
173 a compromise between accuracy and calculation time. For complex particle shapes with convex and
174 concave surfaces, even with a high number of spheres, the approximation is still far from the
175 Computer Aided Design (CAD) model. In order to keep the particles to be simulated as simple as
176 possible, cylindrical shapes with inner holes, such as Raschig rings or multi-hole cylinders, can be
177 described by a full cylinder [37, 38]. After the DEM simulation, the composite particle is transformed
178 back into the original CAD particle shape. This approach was used in these publications for lowering
179 of computational time, since the full-cylinder approximation is made by a fewer number of composite
180 DEM spheres. Since there is a difference in geometry and mass, there might be a difference in bed
181 structure resulting from this approximation. In the presented references, there was no comparison
182 made between the full-cylinder DEM approach and a DEM approximation of a hollow cylinder. For
183 a closer look at the influence of the approximation methods on the bed structure, in this work, a
184 Raschig ring shape was modeled based on a full-cylinder shape and an approximation of the hollow
185 cylinder as shown in Table 1. The differences of porosity and velocity profiles, as well as simulation
186 time will be presented later in the results section.

187 2.1.2 Blender – Rigid Body Approach in Blender

188   Blender has various methods with which fixed beds can be generated. In addition to the rigid
189 body simulation discussed here, it is also possible to consider a soft body approach. However, since
190 this method is very computationally intensive, only the rigid body simulation will be referred to in
191 the following. Rigid bodies are idealized bodies where the distance between each pair of points on
192 the surface of the body never changes, even when forces are applied [23]. While catalyst pellets are
193 from robust materials, it can be assumed that this approach of non-deformation is appropriate. For a
194 comparison between a rigid body and soft body simulation in Blender see [39]. The motion is
195 modeled using the Newton-Euler equations, a system of differential equations based on Newton's

196 laws [23]. The net force **f** acting on the body is equal to the change of the translation momentum
197 ($m \cdot$ **v**) with time (12):

$$\mathbf{f} = \frac{d(m \cdot \mathbf{v})}{dt} \tag{12}$$

198 For the description of the rotation movement, the net moment τ is represented by the change of the
199 rotation moment $(\mathbf{I} \cdot \omega)$ with time (13):

$$\tau = \frac{d(\mathbf{I} \cdot \omega)}{dt} \tag{13}$$

200 The force **f** is the vector sum of all forces acting on the body, while τ is the vector sum of all
201 moments of all forces and pure moments. To describe point contacts between objects, the coulomb
202 friction model is used, which requires contact at a single point. The contact force $\mathbf{f}_c$ is divided into a
203 normal component $\mathbf{f}_n$ and two orthogonal components $\mathbf{f}_t$ and $\mathbf{f}_o$. Similarly, the relative velocities
204 between the contact points are divided into normal and tangential components. A negative speed in
205 the normal direction v_n is not allowed, since this would be accompanied by an overlap of the objects.
206 The coulomb model uses a *Friction Cone*, which can be described by (14). The contact force $\mathbf{f}_n$ is larger
207 than zero, because bodies only press against each other, but do not pull against.

$$F(\mathbf{f}_n, \mu) = \mu^2 \mathbf{f}_n^2 - \mathbf{f}_t^2 - \mathbf{f}_o^2 \tag{14}$$

208 The force depends on the static friction factor μ and the normal force $\mathbf{f}_n$ used in (15) and (16) to
209 calculate the tangential force components $\mathbf{f}_t$ and $\mathbf{f}_o$.

$$\mathbf{f}_t = \frac{-\mu \cdot \mathbf{f}_n \cdot v_t}{\beta} \tag{15}$$

$$\mathbf{f}_o = \frac{-\mu \cdot \mathbf{f}_n \cdot v_o}{\beta} \tag{16}$$

210 The other factors are the tangential velocity components v_t and v_o of velocity at the contact point,
211 which are also used to calculate the sliding speed β (17).

$$\beta = \sqrt{v_t^2 + v_o^2} \tag{17}$$

212 For further information on the theory of rigid body simulation in video-animation programs, see e.g.
213 [23].

214   In contrast to the DEM, where contact forces are calculated based on a sphere, in Blender the
215 contact between objects is calculated based on the actual faces. This leads to the possibility to use the
216 original three dimensional (3D) CAD model for the filling simulation. It has shown that simulation
217 time of Blender is scaling with the number of faces, so that a closer look on geometry approximation
218 is necessary. If the particle geometry comes from a 3D-CAD program, the triangulation of surface
219 mesh is very fine and leads to long simulation times. For this reason, the CAD surface has to be re-
220 meshed in view of the trade-off between exact geometry representation (fine surface mesh) and
221 computational cost (coarse surface mesh). A closer look at different surface triangulations of a sphere
222 gives Figure 1. A sphere generated in Blender shows a total number of 960 triangles (Figure 1 (a)).
223 With STAR-CCM+, the sphere's surface is approximated with 9,408 faces (Figure 1 (b)). Applying the
224 option *Decimate Geometry* in Blender transforms the STAR-CCM+ surface into what is shown in Figure
225 1 (c). This procedure can be also applied in Blender for non-spherical pellets, but might be also
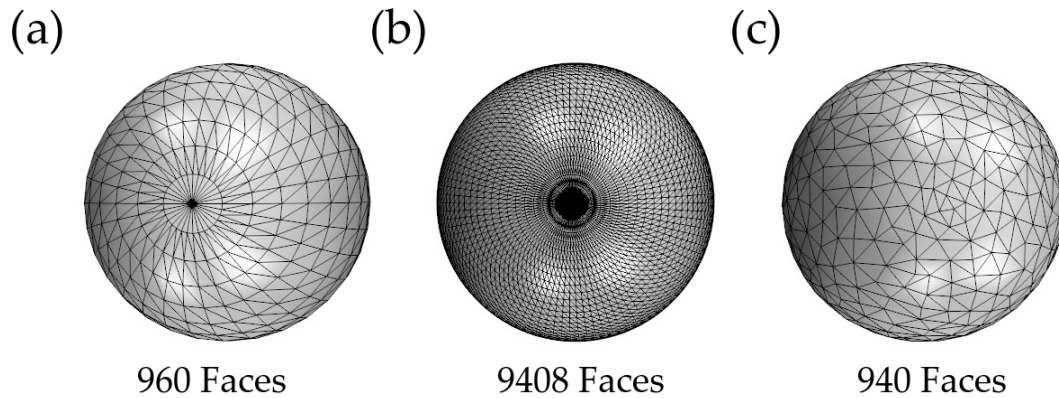226 performed with other CAD software.

(a)   (b)   (c)

960 Faces   9408 Faces   940 Faces

Figure 1. Different surface triangulations of a sphere: (a) Blender, (b) STAR-CCM+, (c) using Blender option *Decimate Geometry* on (b).

While the triangulated sphere from Blender in Figure 1 (a) and the 3D-CAD model sphere from STAR-CCM+ in Figure 1 (b) have an inhomogeneous mesh, where faces get smaller in the direction of the pole, in the decimated geometry (Figure 1 (c)) the triangle faces are equally sized. Such a distributed mesh is preferred, because otherwise the restitution and friction is not independent on the location of contact. The difference of the methods in terms of friction and restitution are the phase interaction approach in DEM and the object based approach in Blender. Friction and restitution can be directly defined for every object created in a Blender scene. For collisions between two objects, the static friction factor μ is calculated by multiplying friction factors of the single objects μ_B. The factor μ_B needs to be calculated from the static friction factor μ, belonging to the considered phase interaction. For the Blender object based friction factor of pellets $\mu_{B-Pellet}$ and container $\mu_{B-Container}$ (18) and (19) were used:

$$\mu_{B-Pellet} = \sqrt{\mu_{Pellet-Pellet}} \tag{18}$$

$$\mu_{B-Container} = \frac{\mu_{Container-Pellet}}{\mu_{B-Pellet}} = \frac{\mu_{Container-Pellet}}{\sqrt{\mu_{Pellet-Pellet}}} \tag{19}$$

In analogy, the coefficient of restitution e is defined in DEM for phase interactions and in Blender for single objects with the (20) and (21):

$$e_{B-Pellet} = \sqrt{e_{Pellet-Pellet}} \tag{20}$$

$$e_{B-Container} = \frac{e_{Container-Pellet}}{e_{B-Pellet}} = \frac{e_{Container-Pellet}}{\sqrt{e_{Pellet-Pellet}}} \tag{21}$$

The formulation in Blender makes it difficult to map more complex systems with more than two materials. The fixed-bed filling process, which only consists of two materials (container and pellets), can be simulated with the help of (20) and (21). A further setting in Blender is the collision margin, which indicates the distance to the object at which the collision should occur. In order to correctly map the collisions between the particles and between particles and the wall, this value must be set to zero, as mentioned from Partopour et al. [27]. Otherwise, the collision does not occur at the surfaces of the bodies. The recommended value in Blender is 40 mm, since the best results were achieved with values greater than zero [40]. In contrast to packed bed-filling processes, collision simulations in typical Blender applications take place at much larger dimensions.

256   *2.2 CFD*

257   2.2.1 Governing Equations

258   Computational fluid dynamics are based on the well-known conservation equations of mass,
259   momentum, energy, and species mass. For details on CFD modeling for fixed-bed reactors, see e.g.
260   Dixon et al. [6] and Jurtz et al. [7]. In this study, only steady-state cold flow CFD simulations were
261   carried out. The conservation of mass is given by:

$$\nabla \cdot (\rho \cdot \mathbf{v}) = 0 \tag{22}$$

262   where ρ is the fluid density and $\mathbf{v}$ is the velocity vector. Furthermore, the conservation of
263   momentum reads:

$$\nabla \cdot (\rho \cdot \mathbf{v} \cdot \mathbf{v}) = \nabla \mathbf{T} \tag{23}$$

264   with $\mathbf{T}$ as the stress tensor described by:

$$\mathbf{T} = -\left(p + \frac{2}{3} \cdot \mu \cdot \nabla \mathbf{v}\right) \cdot \mathbf{I} + 2 \cdot \mu \cdot \mathbf{D} \tag{24}$$

265   and μ as the mixture viscosity and $\mathbf{I}$ as the unit tensor, p being the pressure, and $\mathbf{D}$ is the
266   deformation tensor:

$$\mathbf{D} = \frac{1}{2} \cdot [\nabla \mathbf{v} + (\nabla \mathbf{v})^T] \tag{25}$$

267   2.2.2 Meshing and Solving

268   For analysis of the porosity and local velocity fields all synthetic packed beds are meshed with
269   STAR-CCM+. The Blender generated beds are imported as Standard Triangulation Language (STL)
270   files, a common file format for triangulated surfaces in CAD. The applied mesh properties of STAR-
271   CCM+ are listed in Table 2, using the Base Size as reference for several relative size controls.

272   **Table 2.** Meshing properties in STAR-CCM+.

Base Size	d_p
Target Surface Size	50% *of Base Size*
Minimum Surface Size	4% *of Base Size*
Prism Layer Total Thickness	δ_{BL}(26)

273
274   The Target Surface Size is the face size, which the mesher achieves, when no controls for a smaller
275   mesh are set. In order to capture complex features and allow more refinement, the minimum surface
276   size should be decreased in comparison to the target size.
277   The boundary layer thickness δ_{BL} is calculated according to (26) [41] with the highest simulated
278   particle Reynolds-Number Re_p (27):

$$\delta_{BL} = 1.13 \cdot Re_p^{-0.5} \cdot d_p \tag{26}$$

$$Re_p = \frac{\rho \cdot d_p \cdot v_0}{\eta} \tag{27}$$

279   In order to prevent bad cells in contact regions, local flattening of point, line, and face contacts was
280   applied, as described in earlier works for spheres [42] and for non-spherical particles [38]. A typical
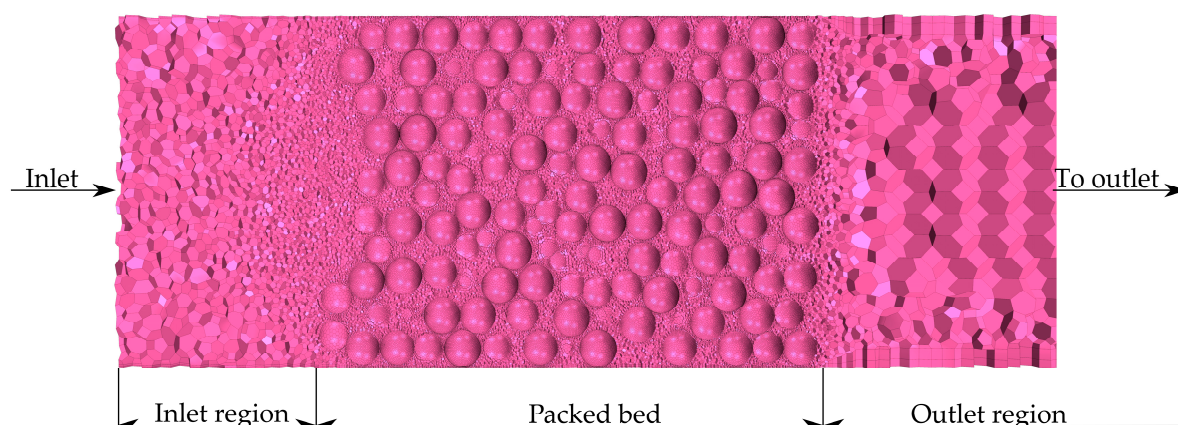281   mesh of a bed of spheres is shown in Figure 2.

Figure 2. Mesh for radial porosity profiles and CFD simulations.

2.2.3 Local Porosity Determination

The porosity calculation is based on the generated volume mesh. The overall porosity of the packed bed is the ratio of the free volume V_{free}, which is interstitial region and likewise the sum of all computational cells, and the volume of the cylindrical container:

$$\varepsilon = \frac{V_{\text{free}}}{\pi \cdot R^2 \cdot h_{\text{Cylinder}}} \tag{28}$$

Experimental data from Giese et al. [30] were used for the validation. The overall porosity $\bar{\varepsilon}$ was extracted from the radial porosity profiles:

$$\bar{\varepsilon}_{\text{Giese}} = \sum_i \frac{A_i(r)}{\left(\sum_i A_i(r)\right)} \cdot \varepsilon_i(r) \tag{29}$$

The theoretical overall porosity was calculated with the equations from Dixon [43]. For the determination of the radial porosity profiles of the simulations, a number of 100 cylindrical planes were placed in the container with equal distances, as seen in Figure 3. The porosity at the radial position r results from the ratio of the free surface A_{free} to the total surface of the cylinder A_{total}, which is calculated with the height of the cylindrical plane $h_{\text{Cylinder Plane}}$:

$$\varepsilon(r) = \frac{A_{\text{free}}}{A_{\text{total}}} = \frac{A_{\text{free}}}{2 \cdot \pi \cdot r \cdot h_{\text{Cylinder Plane}}} \tag{30}$$
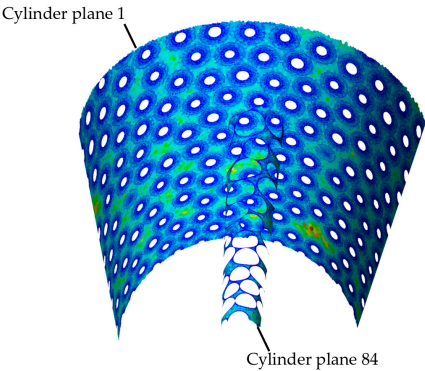
Cylinder plane 1

Cylinder plane 84

297

Figure 3. Cylindrical planes for calculation of radial porosity and velocity profiles.

2.2.4 Local Velocity Profiles

The same cylindrical planes were used to determine the specific radial velocity profiles $v_{\text{specific}}(r)$:

$$v_{\text{specific}}(r) = \frac{\bar{v}_z(r) \cdot \varepsilon(r)}{v_0} \qquad (31)$$

, where $\bar{v}_z(r)$ is the velocity component in z-direction averaged over the cylindrical planes, $\varepsilon(r)$ is the radial porosity profile and v_0 is the inlet superficial velocity.

3. Numerical Setup

In Table 3 the settings of the DEM and rigid body simulations are summarized. As can be seen, not all of the sophisticated DEM models are implemented in Blender. Table 4 shows the geometric dimensions of all generated fixed beds as well as the boundary conditions. Finally, the solver settings are shown in Table 5. The Blender mesh method will be discussed in more detail later on.

310   **Table 3.** Comparison of DEM and Rigid Body settings.

Method	DEM	Rigid Body
Software	• STAR-CCM+	• Blender
Solver settings	• Timestep Δt • Inner Iterations • Maximum Physical Time t_{max}	• Steps per Second with $\Delta t = \dfrac{1}{Steps\ per\ Second}$ • Solver Iterations • Endframe with $t_{\mathrm{max}} = \dfrac{Endframe}{24\frac{Frames}{s}}$
Friction	• Coefficient of friction μ • Adjustable for phase interaction → More than two materials possible	• Coefficient of friction μ_{B} • Conversion with (18 and (19 • More than two materials only possible with compromises
Restitution	• Coefficient of restitution e • "Normal" and "tangential" direction • Adjustable for phase interaction → More than two materials possible	• Coefficient of restitution e_{B} • Conversion with (20 and (21 • More than two materials only possible with compromises
Collision margin	• Not applied	• Set to $d_{\mathrm{Collision}} = 0$ for no gaps • Default setting: $d_{\mathrm{Collision}} = 40$ mm
Damping	• Part of the spring-dashpot model	• Amount of speed that is lost over time • Values for linear and rotational speed adjustable
Density	• Density ρ	• Density ρ for automatic calculation particle mass • Direct input of the mass m of the particles
Young's modulus	• Young's modulus E	• Not applied
Poisson-Number	• Poisson-Number ν	• Not applied
Particle shape	• Spheres • For non-spherical particles: composite particle	• In principle all shapes possible • Selection of a suitable collision shape

311

312   **Table 4.** Boundary conditions of all simulations.

Source	Particle	Dimension	Boundary Conditions
Giese et al. [30]	Sphere	$d_\text{p} = 8.6$ mm $D = 80$ mm	$\mu_\text{Pellet−Pellet} = \mu_\text{Cylinder−Pellet} = 0.9$ $e_\text{Pellet−Pellet} = e_\text{Cylinder−Pellet} = 0.67$
	Cylinder	$d_\text{p} = 8$ mm $h_\text{p} = 8$ mm $D = 80$ mm	
	Raschig ring	$d_\text{outer} = 8$ mm $d_\text{inner} = 6$ mm $h_\text{p} = 8$ mm $D = 80$ mm	
Caulkin et al. [15]	Cylinder	$d_\text{p} = 3.42$ mm $h_\text{p} = 3.46$ mm $D = 44.5$ mm	$\mu_\text{Pellet−Pellet} = \mu_\text{Cylinder−Pellet} = 0.7$ $e_\text{Pellet−Pellet} = e_\text{Cylinder−Pellet} = 0.7$
	Raschig ring	$d_\text{outer} = 4.6$ mm $d_\text{inner} = 2.5$ mm $h_\text{p} = 5$ mm $D_\text{top} = 28$ mm $D_\text{bottom} = 24$ mm	$\mu_\text{Pellet−Pellet} = \mu_\text{Cylinder−Pellet} = 0.9$ $e_\text{Pellet−Pellet} = e_\text{Cylinder−Pellet} = 0.67$
No reference	Complex Particles	$d_\text{p} = 10$ mm $r_\text{inv} = 0.568$ mm $r_\text{env} = 1$ mm $D = 80$ mm	$\mu_\text{Pellet−Pellet} = \mu_\text{Cylinder−Pellet} = 0.7$ $e_\text{Pellet−Pellet} = e_\text{Cylinder−Pellet} = 0.7$

313

314   **Table 5**. Solver Settings for packing generation.

Source	Particle	Packing Generation		
		Time Step	Solver Itterations	Number of Particles
Giese et al. [30]	Sphere	$\Delta t = 0.001$ s	2	1000
	Cylinder			
	Raschig Ring			
Caulkin et al. [15]	Cylinder	$\Delta t = 0.001$ s	2	1500
	Raschig Ring			310
No reference	Complex Particles	$\Delta t = 0.001$ s Blender Mesh: $\Delta t = 0.00025$ s	2 Blender Mesh: 10	1000

315

316   **4. Results**

317   *4.1 Overall Porosity*

318   The porosity for different particle shapes is compared between simulations, experimental data
319   from Giese et al. [30] and correlations from Dixon [43], see Figure 4. The overall agreement between
320   experimental data and simulation is satisfactory. DEM shows in general a slightly smaller porosity
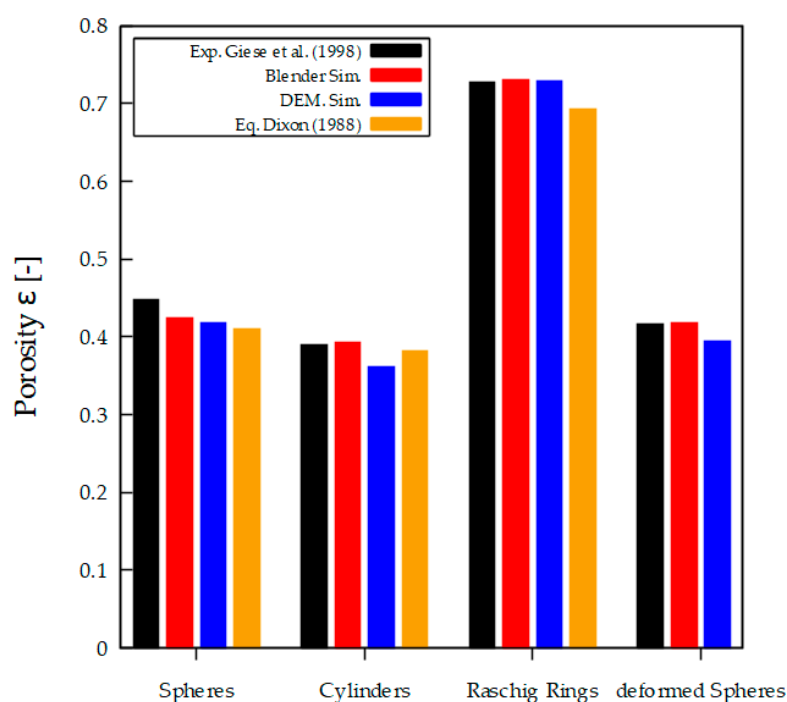321   than Blender, with a pronounced difference for beds made of cylinders.

322

323   **Figure 4.** Overall porosity of fixed beds made of different particle shapes. Experiments from Giese et
324   al. [30]. Equations from Dixon [43].

325   *4.2 Spheres*

326   A packed bed of 1,000 spheres was generated with STAR-CCM+ and Blender. Both beds were
327   meshed in STAR-CCM+ with equal properties for calculation of radial porosity and CFD simulations.
328   The injection method for both approaches however was slightly different. For DEM spheres were
329   injected at a single point with a frequency of $100\,s^{-1}$ and a velocity in z-direction of $1\,m\,s^{-1}$. This is
330   more or less similar to the injection method in Blender. All particles were lined up at the beginning
331   of the simulation above the cylindrical container. The Blender simulation also needed a physical time
332   of $10\,s$ for all particles to inject. Since glass beads were used in the original experiments, the
333   corresponding physical properties were set in Blender and STAR-CCM+, see Table 4. The obtained
334   packed beds are shown in Figure 5 (a) as 3D CAD model and in (b) in terms of the radial porosity
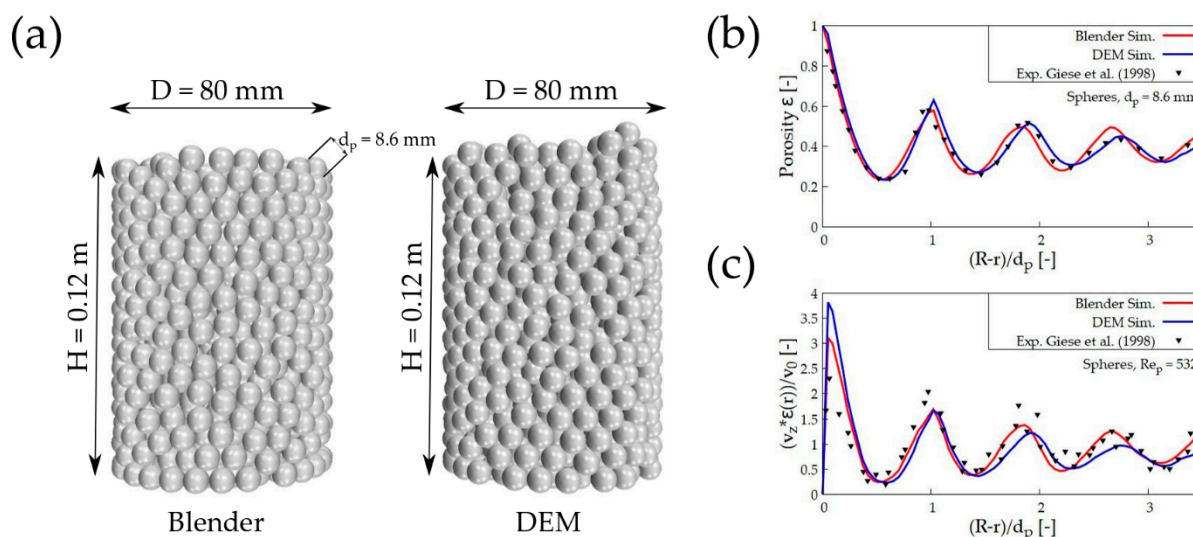335   and (c) radial velocity profiles.

Figure 5. (a) Comparison between synthetic generated packings of spheres, (b) radial porosity profiles, and (c) velocity profiles. Experiments from Giese et al. [30].

Both generated beds have an optical consistency with the same bed height. The overall porosity in Figure 4 shows a good agreement for the two synthetic packing methods, which result in a porosity lower than the experimental data but higher than in the theoretical equations. The radial porosity profile on Figure 5 (b) of both methods are in excellent agreement with the experimental data from Giese et al. [30]. This can be shown with the coefficient of determination R^2 for the parity chart as a comparison between simulation data from both methods and experimental data. The coefficients of determination $R^2_{\text{Blender}} = 0.92$ and $R^2_{\text{DEM}} = 0.91$ are similar and show good agreement with the data. The velocity profiles (Figure 5 (c)) follow the porosity profiles. Since the Blender bed is slightly looser, the near-wall maximum velocity (wall channeling) is slightly smaller than for the DEM bed.

4.3 Cylinders

Non-spherical pellets are widely used in industrial applications. Among those, the most simple shape is a cylinder. Based on two different experimental studies, beds made from cylinders were investigated with both generation methods. Firstly, experiments from Giese et al. [30] were reproduced synthetically with the same number of cylinders, see Figure 6 (a) for a visual comparison between Blender and STAR-CCM+. The DEM bed shows a lower height than the Blender bed. This is also reflected in the lower overall porosity in Figure 4. It can be also seen that the radial porosity of the DEM bed is constantly below the Blender-generated bed (Figure 6 (b)). Consequently, the velocity of the CFD simulation of DEM bed is higher in the near-wall region. One explanation of the overall lower porosity is the approximation of the cylinder shape in the DEM with the composite particle approach. This approximation leads to a deviation in comparison to the CAD particle especially at the edges of the cylinder. A closer look at this phenomenon gives Figure 7. Although in the DEM bed there are no overlaps of the composite particles, the transformation back to the CAD particles leads to overlaps in the STL file. This leads to a denser bed than in the Blender case, where there are no overlaps detected in the bed generation simulation, see Figure 7 right-hand side. These overlaps can be treated with the unite method or the caps method as was described in detail in Ref. [44].
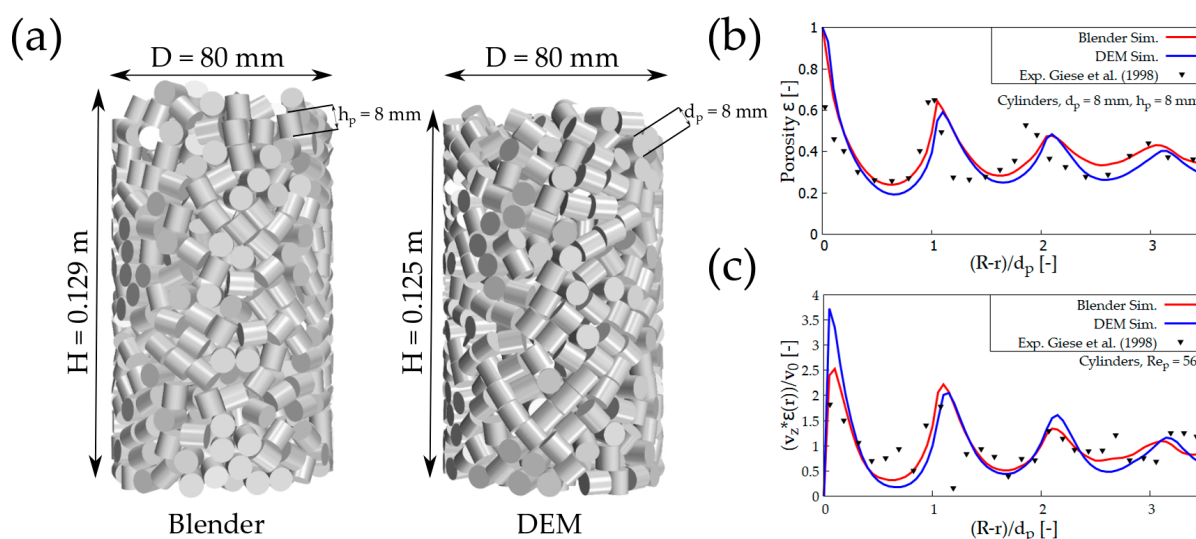
Figure 6. (a) Comparison between synthetic generated packing's of cylinders, (b) radial porosity profiles, and (c) velocity profiles. Experiments from Giese et al. [30].
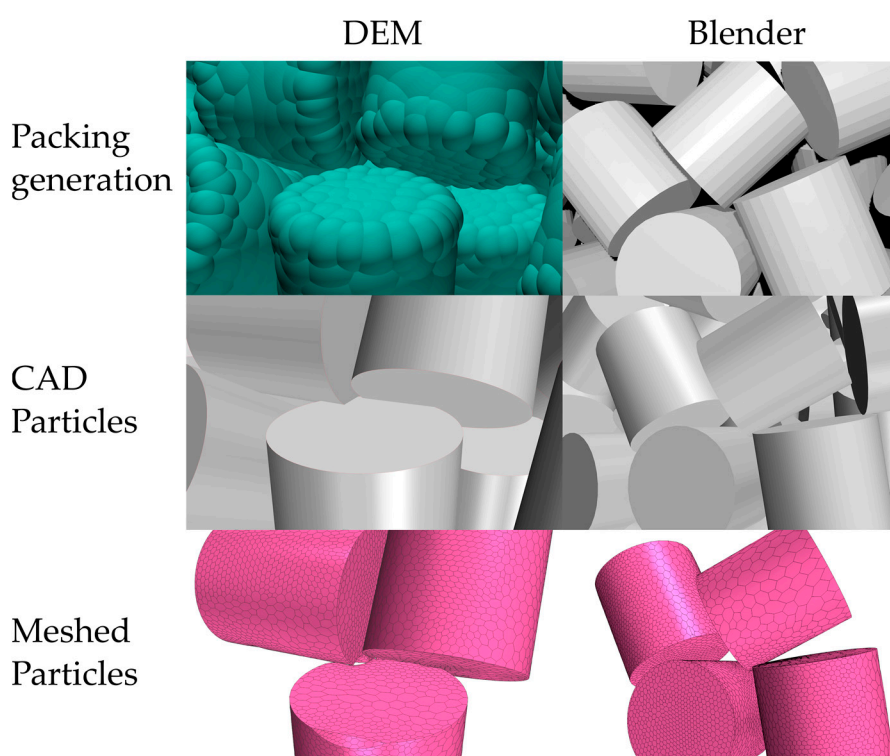
Figure 7. Bed generation with DEM (left) and rigid body (right), CAD particle transformation, and resulting mesh.

At this point, the results show that the rigid body approach has advantages over DEM for the simulation of complex particle geometries. In addition, the agreement of the Blender simulation can be expressed by the coefficient of determination for the local porosity profile $R^2_{\text{Blender}} = 0.41$, which is larger than for the generated bed from DEM $R^2_{\text{DEM}} = 0.29$. There is a slight shift of the oscillating porosity profile of the simulations compared to the experimental data. This is one reason why the R^2 values are lower than for spheres, cf. Figure 6 (b). Nevertheless, the porosity profile maxima and minima are in a similar range. Another important aspect of packed bed morphology is the particle orientation. Particle-orientation distribution was evaluated experimentally with computer

378   tomography (CT) data by Caulkin et al. [15]. This data set is compared with synthetically generated
379   beds of Blender and STAR-CCM+ in Figure 8.

380

381   **Figure 8.** (a) Comparison between synthetic generated packing's of cylinders, (b) radial density
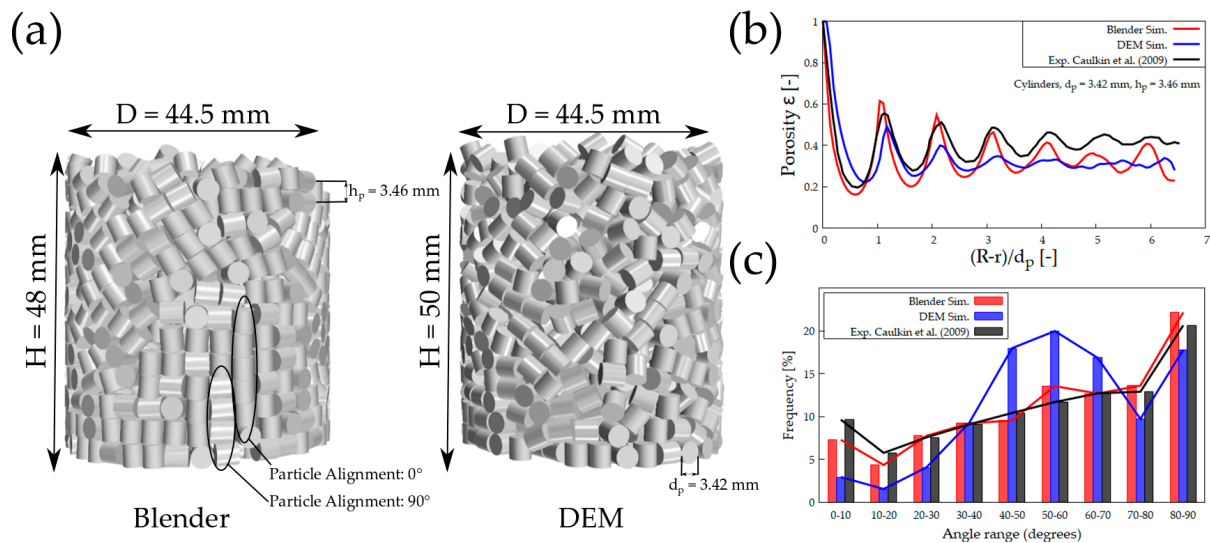382   distribution, and (c) particle alignment. Experiments from Caulkin et al. [15].

383   The optical height of the generated beds in Figure 8 (a) is not exactly similar, however the near-
384   wall particles show different orientations. In the Blender bed the cylinders stack over each other,
385   while in the DEM bed most of the cylinders are inclined. The porosity profile of the Blender bed is
386   more pronounced than the DEM bed and furthermore lower than the DEM bed (Figure 8 (b)). This is
387   different to the observation of the particle bed in Figure 6 (b) where Blender has a higher porosity
388   than the DEM bed. The particle arrangement in Figure 8 (c) shows differences between the two
389   synthetic methods. The angle range is calculated for an angle in comparison to the normal z-direction.
390   An angle of 0° is a standing cylinder, while 90° is a horizontally oriented cylinder. The Blender bed
391   is characterized by a higher frequency of stacked particles, as already noticed in Figure 8 (a). In
392   addition, the alignment of DEM particles shows a higher frequency for particles from 40° to 70°. The
393   comparison with experimental data from Caulkin et al. [15] shows an acceptable agreement with the
394   Blender bed (Figure 8 (c)). For many applications, the near-wall region is of great interest, e.g. due to
395   critical radial heat transfer from the wall to the gas etc. Therefore, a closer look at the bed morphology
396   in this region is crucial. Figure 9 (a) shows one layer of particles close to the container wall for a
397   Blender bed and a STAR-CCM+ bed. The Blender particles arrange either standing or lying resulting
398   in more particles fitting into the outer ring. On the contrary, the DEM bed is characterized by a looser
399   morphology and therefore more particles with angles in the mid-range, cf. Figure 9 (b). The alignment
400   of the Blender cylinders shows a significantly higher frequency in the range up to 30 degrees than
401   with the DEM. This observation shows why the fixed bed from Blender has a lower bed height and a
402   lower porosity than the DEM bed (Figure 8 (a)), despite the fact of overlapping particles.
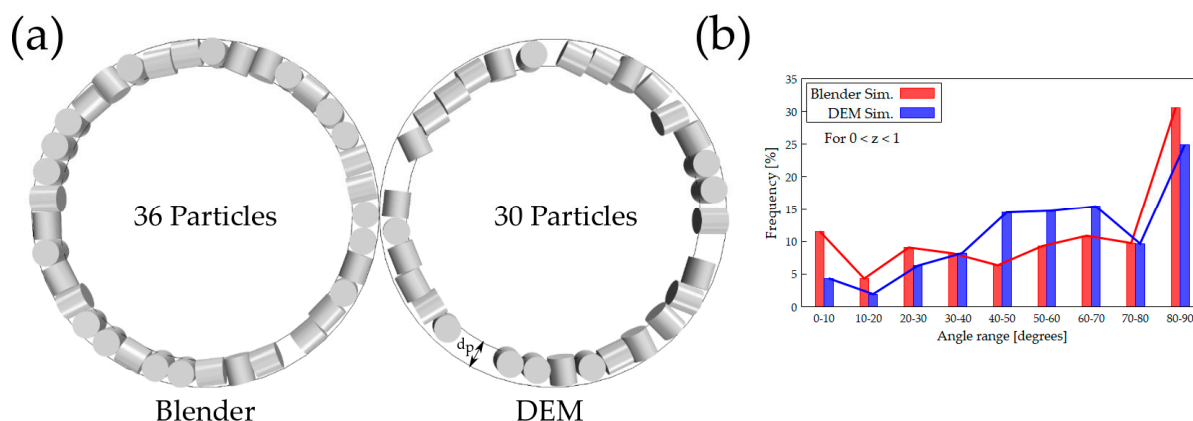403
404

Figure 9. (a) One layer of cylinders touching the container wall. (b) Orientation distribution of near-wall cylinders.

4.4 Raschig Rings

Another frequently used particle shape is the Raschig ring. In this study, the approximation of a Raschig ring with the composite approach is compared against a full cylinder, as well as the rigid approach. The advantage of the full cylinder approximation is that a smaller amount of composite spheres is needed, cf. Table 1. The number of spheres can be reduced from 449 to only 100 per particle. By using a full cylinder, it is possible to generate with only one DEM simulation a certain amount of different particle shapes by transforming the cylinders into rings or more hole cylinders [37, 38]. It can be doubted that the different ballistics of a full cylinder and a one-hole cylinder give similar bed morphologies. In addition, the packing density between these methods might be different, because the additional free space inside the hollow cylinders can be filled with edges of other particles. In Figure 10 the comparison between Blender, full cylinder DEM, and "ring" DEM, as shown in Table 1, against experimental data is shown. In Figure 10 (a) only the Blender bed and ring DEM is shown for brevity reasons. Again, the two differently generated beds show similar heights, but different particle orientation.
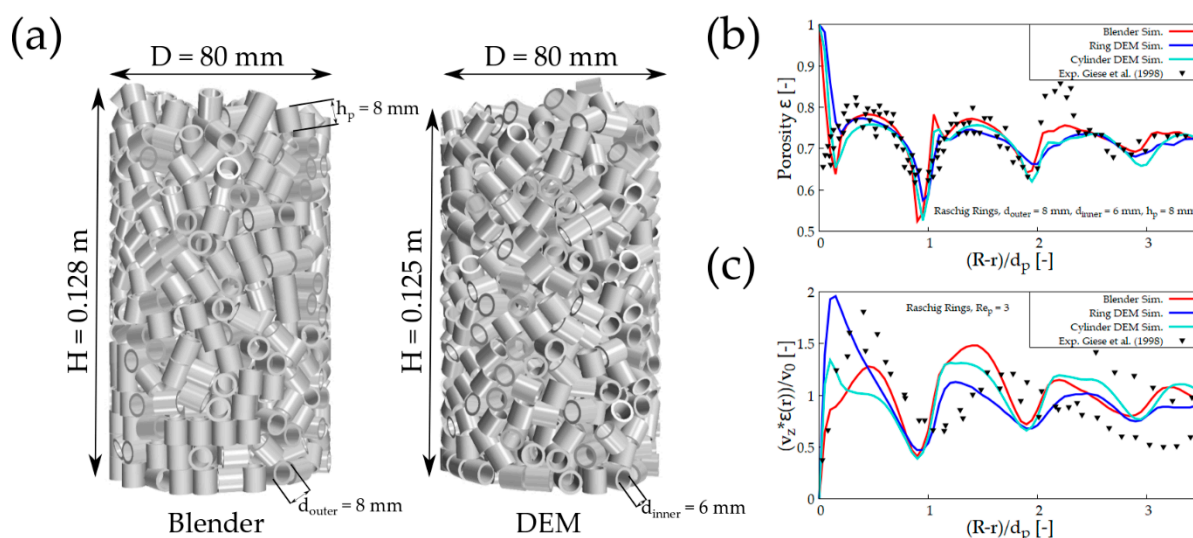

Figure 10. (a) Comparison between synthetic generated packing's of Raschig Rings, (b) radial porosity profiles, and (c) velocity profiles. Experiments from Giese et al. [30].

It can be seen, that the Blender Bed porosity in the near wall region shows a low deviation from experimental data (Figure 10 (b)). Reasons for this will be presented later, where different Blender

427 simulation methods will be presented. In addition, the ring DEM has lower maxima and minima and
428 represents the experimental data in near-wall regions rather well. A difference in experimental data
429 and all three simulations can be seen at a wall distance of $z = 2$, where the results of experiments are
430 larger than simulation predictions. The values of determination for this case are $R^2_{\text{Blender}} = 0.40$ for
431 Blender Simulation, $R^2_{\text{Cylinder DEM}} = 0.22$ and $R^2_{\text{Ring DEM}} = 0.11$. One of the reasons for the large
432 deviation is also the wide scattering of the experimental data as shown in Figure 10 (b). For the fluid
433 simulation (Figure 10 (c)), a large difference between the three methods can be noticed especially in
434 the near-wall region. This leads to assumption that the particle orientation have to be different.

435 An additional bed setup from Caulkin et al. [15] was used to evaluate the orientation of the
436 particles. Notice that the dimensions are different. Again, synthetic beds with Blender and the two
437 DEM methods were generated and compared. In Figure 11 (a) the Blender and DEM bed are shown
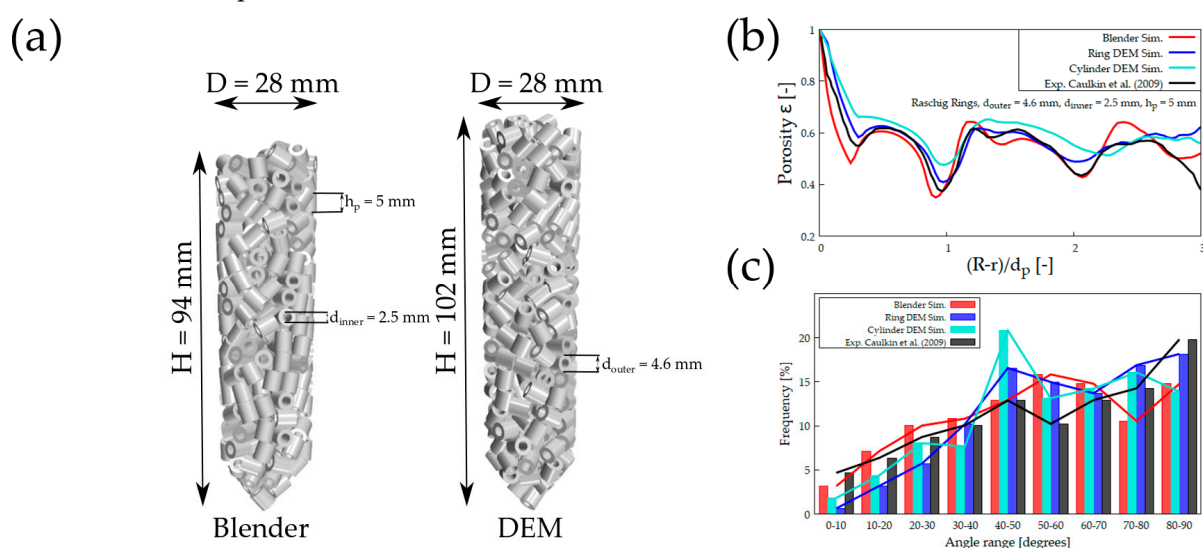438 for illustrative comparison.

439

440 **Figure 11.** (a) Comparison between synthetic generated packing's of Rachig Rings, (b) radial density
441 distribution, and (c) particle alignment. Experiments from Caulkin et al. [15].

442 The radial porosity profile (Figure 11 (b)) shows that the data from Blender and the DEM ring
443 simulation have a small deviation from the experimental data. The DEM generated with the full
444 cylinder composite particles shows a strong deviation in the value at the minimum at $z = 1$. In
445 addition, the porosity of this bed is steadily higher than the data of the others. A glance at the
446 alignment of the particles in Figure 11 (c) shows that the general trend is well captured by the
447 simulations. This time the Blender and ring DEM bed shows similar particle orientation to the
448 experiments. The data of the cylinder DEM, on the other hand, show a strong deviation in which the
449 majority of the particles have an angle between 40° and 50°. The coefficients of determination are
450 listed in Table 6 for the different particle shapes and as summarized as a total value over all Blender
451 and DEM simulations.

452 Table 6. Coefficients of determination

	R^2	
	Blender	DEM
Spheres	0.92	0.91
Cylinders	0.41	0.29
Raschig rings	0.40	0.22*, 0.11+
Total	0.87	0.79

453 *Cylinder DEM, +Ring DEM

454   *4.5 Complex Particles*

455   The filling process of complex particles is challenging due to the difficult particle approximation
456   for the DEM composite approach and due to collision detection. A further comparison between
457   Blender and the DEM is conducted with a complex particle shape. For this purpose, a previously
458   unmentioned setting within Blender will be discussed at first. In Blender's rigid body approach,
459   different collision shapes can be selected, which affects the detection of the collision. Commonly in
460   Blender, the convex hull method is applied. With this option, a convex approximation is drawn
461   around the particle for collision detection. Advantage of this method is the high performance and
462   simulation stability. However, the convex hull method cannot be used to represent a cylinder with
463   curved outer surface. As shown in Figure 12 (a), a small object will collide with the pellet at the dashed
464   position for the convex hull method. Another collision shape in Blender is the mesh method, which
465   is based on the real shape of object [40]. For the mesh method in Figure 12 (b), the collision detection
466   takes place at the correct surface of the particle.

467
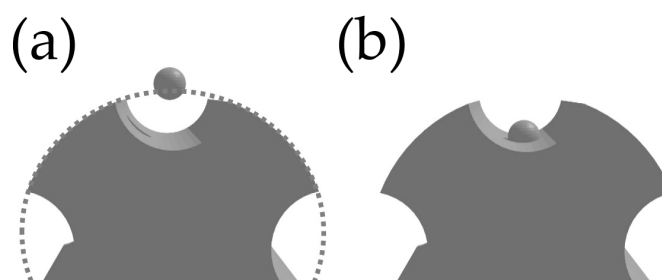
468   **Figure 12.** Different collision shapes in Blender. (a) Convex Hull Method and (b) Mesh Method.

469   Since the complex particle shown in Table 1 has a more complex shape, a simulation based on
470   the mesh collision method should be considered. However, the disadvantage of this method is the
471   much longer simulation time and the instability of the solution [40]. In order to consider the
472   differences, synthetic beds with both Blender methods and with the DEM are presented. The
473   composite particle method used in the DEM corresponds to the composite maximum shown in Table
474   1.

475
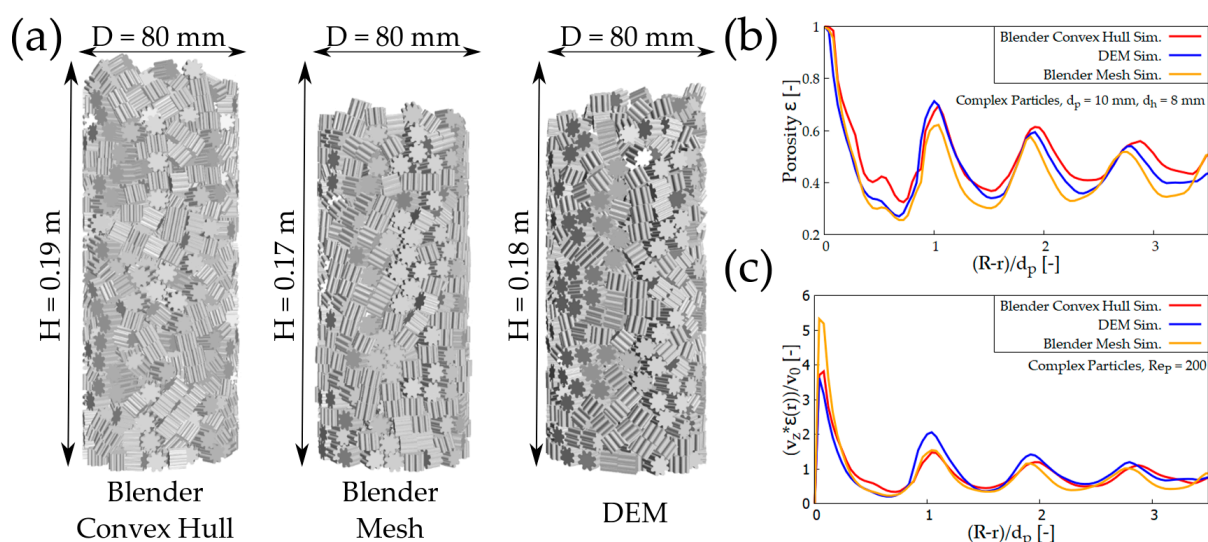
476   **Figure 13.** (a) Comparison between synthetic generated packing's of complex particles, (b) radial
477   porosity profiles, and (c) velocity profiles.

478   The resulting beds in Figure 13 show different heights. The convex hull method yields a
479   significantly higher bed than the mesh method. The reason for this is that the gearwheel-shaped
480   pellets can interlock. The bed generated with DEM, on the other hand, has only a minimally larger

481 height. This optical observation is proven with the radial porosity profile shown in Figure 13 (b). The
482 convex hull method profile shows a difference in velocity for the near-wall region. The results
483 highlight that the convex hull method applied for such complex particles leads to unrealistic loose
484 packings. However, the solution stability is more robust than for the mesh collision method.

485 *4.6 Simulation Time*

486   A further criterion for the selection of synthetic packed bed generation is the total simulation
487 time. Since the DEM scales with the number of spheres for the composite particle, the simulation time
488 is in general longer for particles that are more complex. Figure 14 summarizes the calculation time
489 on one CPU (Intel Xeon x5660) of all simulations. In general, Blender shows shorter simulation times
490 in comparison to DEM. While the time increases with the DEM when changing from spheres to
491 cylinders, it decreases with Blender. This can be explained by the fact that Blender scales with the
492 number of surfaces of the particles. Since more surfaces are required for a sphere than for a cylinder,
493 the simulation time is shorter. The time of Raschig rings is shown for ring DEM. Time savings are
494 possible by using a simple cylinder, leading to the same simulation time as the shown cylinders. In
495 Figure 14 (a) it can be seen that the time advantage of Blender is getting higher with the complexity
496 of the particle shape. While for spheres the DEM time is nearly doubled, for Raschig rings it is 26
497 times larger than Blender. Due to the stable and fast simulation, the Blender method convex hull
498 method was used for the particles shown on the left. Since this method is no longer suitable for
499 complex particles, the slower mesh method was shown here. Nevertheless, for these complex
500 particles, which are difficult to represent, the Blender Mesh simulation is clearly 13 times faster than
501 STAR-CCM+.
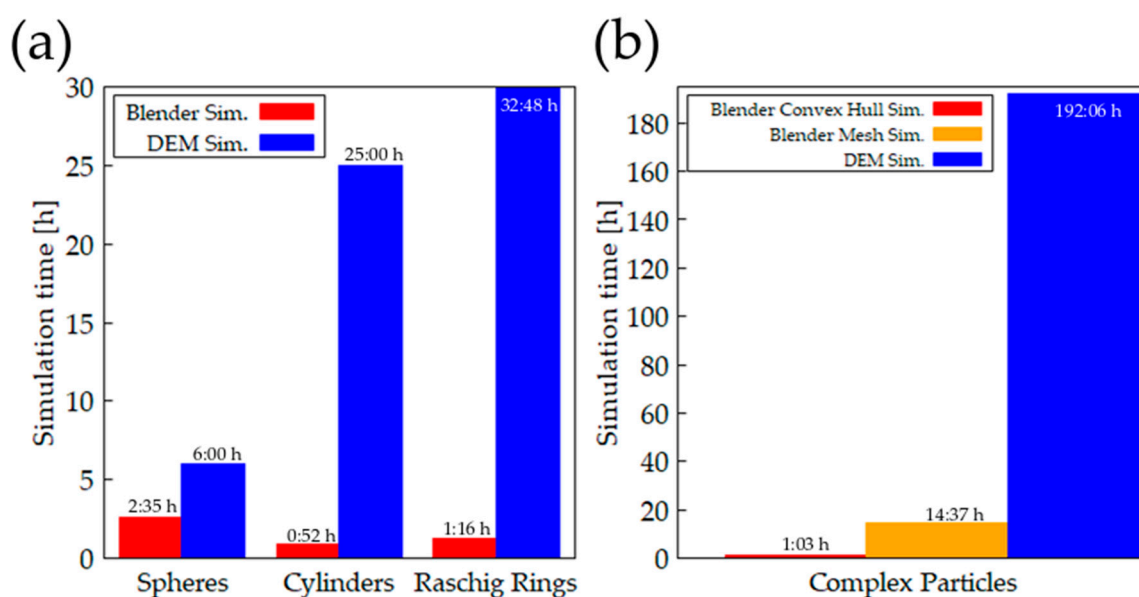
503   **Figure 14.** Simulation Time of Blender and DEM for different particle shapes.

504 **5. Conclusion**

505   In particle-resolved CFD simulations of fixed-bed reactors, the underlying bed morphology
506 plays a paramount role. Synthetic bed-generation methods are much more flexible and faster than
507 image-based approaches. Typical decision aspects for synthetic bed generators are: realistic bed
508 structure generation (accuracy against experimental data), easy-to-handle use, exportability of bed
509 structure, flexibility for different shapes, physically relevant models, and finally low computational
510 costs. In this study, we looked critically at the commonly used DEM approach and compared the
511 resulting bed morphology with the more recently presented rigid-body method incorporated into the
512 Blender software.

513   Both methods show a large flexibility for different particle shapes originating from an external
514   CAD modeler and the option to export the particle bed via the STL format. In addition, both methods
515   come with a graphical user interface, which is easy-to-use and furthermore automation processes can
516   be included, i.e. python for Blender and Java scripting for STAR-CCM+. Whereas the commercially
517   available STAR-CCM+ software is well documented in the own user guide and own internet forum,
518   the documentation of the open-source bullet physics is rather vague. However, both methods show
519   physically meaningful models to simulate the filling process of fixed-bed reactors, whereas the soft-
520   body approach in STAR-CCM+ is more sophisticated than the rigid-body model. In terms of accuracy,
521   the picture is less clear. Both models can predict experimental porosity profiles with satisfactory
522   accuracy, cf. Table 6 for R^2 values between synthetically generated beds and experimental data.
523   Particle orientation is captured more accurately with Blender. However, the experimental data basis
524   is rather scarce. The main disadvantage of the DEM is the approximation of non-spherical particles
525   with the composite particle approach. This approximation can lead in general to denser beds and to
526   overlaps of particles, which in turn results in meshing challenges. Additionally, it was shown that
527   the use of a full-cylinder DEM approximating a Raschig ring leads to differences in the bed structure
528   and the velocity profile, especially due to different pellet orientation. For more complex particle
529   shapes, the fast but simple convex hull collision method in Blender clearly shows its limits. The mesh
530   collision method in Blender resolves the actual particle shape, which requires additional
531   computational costs. Still, Blender is in general clearly faster for the bed generation process,
532   especially, when the complexity of the particle is high, cf. Figure 14.

533   Future studies should incorporate experimental data from complex particle shapes in order to
534   judge on the accuracy of the different collision methods in Blender. In addition, special attention
535   should be drawn to the damping forces applied to the moving particles, since this can violate the law
536   of conservation of linear and angular momentum and energy over each time.
537

538 **Nomenclature**

539 *Latin Letters*

A	area	(m^2)
d	overlaps	(m)
d_p	particle diameter	(m)
D	tube diameter	(m)
$\mathbf{D}$	deformation tensor	(−)
e_N	coefficient of restitution	(−)
E_{eq}	equivalent Young´s modulus	(Pa)
$\mathbf{f}$	force (rigid body approach)	(N)
F	force (soft body approach)	(N)
$\mathbf{F}_b$	body force	(N)
$\mathbf{F}_c$	contact force	(N)
$\mathbf{F}_g$	gravity force	(N)
$\mathbf{F}_s$	surface force	(N)
h	height	(m)
I	moment of inertia	($kg \cdot m^2$)
$\mathbf{I}$	unit tensor	(−)
K	spring stiffness	(kg/s^2)
m	mass	(kg)
M_{eq}	equivalent particle mass	(kg)
$\mathbf{n}$	unit normal vector	(−)
N	tube-to-particle-diameter ratio	(−)
N	damping	(kg/s)
N_{N-damp}	damping coefficient	(−)
p	pressure	(Pa)
R	radius	(m)
R^2	coefficient of determination	(−)
Re	Reynolds number	(−)
R_{eq}	equivalent radius	(m)
r	radius of radial position	(m)
$\mathbf{t}$	unit normal vector	(−)
t	time	(s)
T	stress tensor	(Pa)
v	velocity	(m/s)
$\mathbf{v}$	velocity	(m/s)
V	volume	(m^3)

540

541 *Greek Letters*

β	sliding speed	(m/s)
δ_{BL}	Boundary layer thickness	(m)
δ_{max}	maximum overlap	(m)
ε	porosity	(−)
η	dynamic viscosity	($Pa \cdot s$)
μ	static friction coefficient	(−)
ρ	density	(kg/m^3)
τ	net moment	($N \cdot m/rad$)
ω	angular velocity	(rad/s)

542

543   *Subscripts*

0	inlet
Blender	data obtained by the use of Blender
B − Pellet	Blender object based pellet interaction
B − Container	Blender object based container interaction
Container − Pellet	Phase based container-pellet interaction
Cylinder	part: Cylinder
Cylinder Plane	part: Cylinder Plane
DEM	Data obtained by the use of DEM
free	amount of free space or volume
Giese	experimental data taken from Giese et al. (1998)
Pellet − Pellet	phase based pellet interaction
n	normal direction
t	tangential direction
total	amount of total space or volume
p	particle
o	additional tangential direction
specific	specific radial velocity

544

545   *Abbreviations*

3D	3-dimensional
DEM	Discrete Element Method
CAD	Computer Aided Design
CFD	Computational Fluid Dynamics
CT	Computer Tomography
MRI	Magnetic Resonance Imaging
STL	Standard Triangulation Language

546

549   **References**

550   1.   Froment, G. F., Ed. Analysis and Design of Fixed Bed Catalytic ReactorsChemical Reaction Engineering,
551   Bischoff, K. B; AMERICAN CHEMICAL SOCIETY **1972**. *109*, 1-55.

552   2.   Kulkarni, B. d. and Doraiswamy, L. K. Estimation of Effective Transport Properties in Packed Bed Reactors.
553   *Catalysis Reviews* **1980**. *22*, 431–483. DOI=10.1080/03602458008067540.

554   3.   Eisfeld, B. and Schnitzlein, K. The influence of confining walls on the pressure drop in packed beds.
555   *Chemical Engineering Science* **2001**. *56*, 4321–4329. DOI=10.1016/S0009-2509(00)00533-9.

556   4.   Andersson, K. E. B. Pressure drop in packed beds. *Trans. Royal Inst. Technol. Stockholm* **1963**. *201*.

557   5.   Dixon, A. G. Fixed bed catalytic reactor modelling-the radial heat transfer problem. *Can. J. Chem. Eng.* **2012**.
558   *90*, 507–527. DOI=10.1002/cjce.21630.

559   6.   Dixon, A. G., Nijemeisland, M., and Stitt, E. H. **2006**. Packed Tubular Reactor Modeling and Catalyst Design
560   using Computational Fluid Dynamics. In *Advances in Chemical Engineering*, G. B. Marin, Ed. Advances in
561   Chemical Engineering v.31. Elsevier textbooks, s.l., 307–389. DOI=10.1016/S0065-2377(06)31005-8.

562   7.   Jurtz, N., Kraume, M., and Wehinger, G. D. Advances in fixed-bed reactor modeling using particle-resolved
563   computational fluid dynamics (CFD). *Reviews in Chemical Engineering* **2018**. *0*, 87. DOI=10.1515/revce-2017-
564   0059.

565   8.   Wang, Z., Afacan, A., Nandakumar, K., and Chuang, K. T. Porosity distribution in random packed columns
566   by gamma ray tomography. *Chemical Engineering and Processing: Process Intensification* **2001**. *40*, 209–219.
567   DOI=10.1016/S0255-2701(00)00108-2.

568   9.   Baker, M. J., Young, P. G., and Tabor, G. R. Image based meshing of packed beds of cylinders at low aspect
569   ratios using 3d MRI coupled with computational fluid dynamics. *Computers & Chemical Engineering* **2011**.
570   *35*, 1969–1977. DOI=10.1016/j.compchemeng.2011.03.017.

571   10. Hofmann, S., Bufe, A., Brenner, G., and Turek, T. Pressure drop study on packings of differently shaped
572   particles in milli-structured channels. *Chemical Engineering Science* **2016**. *155*, 376–385.
573   DOI=10.1016/j.ces.2016.08.011.

574   11. Zeiser, T., Steven, M., Freund, H., Lammers, P., Brenner, G., Durst, F., and Bernsdorf, J. Analysis of the flow
575   field and pressure drop in fixed-bed reactors with the help of lattice Boltzmann simulations. *Philosophical*
576   *transactions. Series A, Mathematical, physical, and engineering sciences* **2002**. *360*, 507–520.
577   DOI=10.1098/rsta.2001.0945.

578   12. Caulkin, R., Fairweather, M., Jia, X., Gopinathan, N., and Williams, R. A. An investigation of packed
579   columns using a digital packing algorithm. *Computers & Chemical Engineering* **2006**. *30*, 1178–1188.
580   DOI=10.1016/j.compchemeng.2006.02.019.

581   13. Caulkin, R., Ahmad, A., Fairweather, M., Jia, X., and Williams, R. A. An investigation of sphere packed
582   shell-side columns using a digital packing algorithm. *Computers & Chemical Engineering* **2007**. *31*, 1715–1724.
583   DOI=10.1016/j.compchemeng.2007.03.014.

584   14. Caulkin, R., Jia, X., Fairweather, M., and Williams, R. A. Lattice approaches to packed column simulations.
585   *Particuology* **2008**. *6*, 404–411. DOI=10.1016/j.partic.2008.07.022.

586   15. Caulkin, R., Jia, X., Xu, C., Fairweather, M., Williams, R. A., Stitt, H., Nijemeisland, M., Aferka, S., Crine,
587   M., Léonard, A., Toye, D., and Marchot, P. Simulations of Structures in Packed Columns and Validation by
588   X-ray Tomography. *Ind. Eng. Chem. Res.* **2009**. *48*, 202–213. DOI=10.1021/ie800033a.

589   16. Cundall, P. A. and Strack, O. D. L. A discrete numerical model for granular assemblies. *Géotechnique* **1979**.
590   *29*, 47–65. DOI=10.1680/geot.1979.29.1.47.

591   17. Wehinger, G. D. and Kraume, M. CFD als Designtool für Festbettreaktoren mit kleinem Rohr-zu-
592   Pelletdurchmesser-Verhältnis: Heute oder in Zukunft? *Chemie Ingenieur Technik* **2017**. *89*, 447–453.
593   DOI=10.1002/cite.201600155.

594   18. Favier, J. F., Abbaspour-Fard, M. H., Kremmer, M., and Raji, A. O. Shape representation of axi-symmetrical,
595   non-spherical particles in discrete element simulation using multi-element model particles. *Engineering*
596   *Computations* **1999**. *16*, 467–480. DOI=10.1108/02644409910271894.

597   19. Marigo, M. and Stitt, E. H. Discrete Element Method (DEM) for Industrial Applications: Comments on
598   Calibration and Validation for the Modelling of Cylindrical Pellets. *KONA* **2015**. *32*, 236–252.
599   DOI=10.14356/kona.2015016.

600   20. Kodam, M., Bharadwaj, R., Curtis, J., Hancock, B., and Wassgren, C. Cylindrical object contact detection for
601   use in discrete element method simulations, Part II—Experimental validation. *Chemical Engineering Science*
602   **2010**. *65*, 5863–5871. DOI=10.1016/j.ces.2010.08.007.

603   21. Kodam, M., Bharadwaj, R., Curtis, J., Hancock, B., and Wassgren, C. Cylindrical object contact detection for
604   use in discrete element method simulations. Part I – Contact detection algorithms. *Chemical Engineering*
605   *Science* **2010**. *65*, 5852–5862. DOI=10.1016/j.ces.2010.08.006.

606   22. Feng, Y. T., Han, K., and Owen, D.R.J. A generic contact detection framework for cylindrical particles in
607   discrete element modelling. *Computer Methods in Applied Mechanics and Engineering* **2017**. *315*, 632–651.
608   DOI=10.1016/j.cma.2016.11.001.

609   23. Bender, J., Erleben, K., and Trinkle, J. Interactive Simulation of Rigid Body Dynamics in Computer
610   Graphics. *Computer Graphics Forum* **2014**. *33*, 246–270. DOI=10.1111/cgf.12272.

611   24. Blender Org. Manual Homepage. Available online: https://docs.blender.org/manual/en/latest/
612   game_engine/physics/introduction.html (accessed on 26 March 2019).

613   25. Boccardo, G., Del Plato, L., Marchisio, D., Augier, F., Haroun, Y., Ferre, D., and Icardi, M. Pore-scale
614   simulation of fluid flow in packed-bed reactors via Rigid-Body simulations and CFD, 10th International
615   Conference on CFD in Oil & Gas, Metallurgical and process Industries SINTEF, Trondheim, Norway, 17-
616   19th June 2014.

617   26. Boccardo, G., Augier, F., Haroun, Y., Ferré, D., and Marchisio, D. L. Validation of a novel open-source
618   work-flow for the simulation of packed-bed reactors. *Chemical Engineering Journal* **2015**. *279*, 809–820.
619   DOI=10.1016/j.cej.2015.05.032.

620   27. Partopour, B. and Dixon, A. G. An integrated workflow for resolved-particle packed bed models with
621   complex particle shapes. *Powder Technology* **2017**. *322*, 258–272. DOI=10.1016/j.powtec.2017.09.009.

28. Fernengel, J., Habla, F., and Hinrichsen, O. Scripting as an Approach to Automated CFD Simulation for Packed Bed Catalytic Reactor Modeling. *Chemie Ingenieur Technik* **2018**. *90*, 685–689. DOI=10.1002/cite.201700153.

29. Pavlišič, A., Ceglar, R., Pohar, A., and Likozar, B. Comparison of computational fluid dynamics (CFD) and pressure drop correlations in laminar flow regime for packed bed reactors and columns. *Powder Technology* **2018**. *328*, 130–139. DOI=10.1016/j.powtec.2018.01.029.

30. Giese, M., Rottschäfer, K., and Vortmeyer, D. Measured and modeled superficial flow profiles in packed beds with liquid flow. *AIChE J.* **1998**. *44*, 484–490. DOI=10.1002/aic.690440225.

31. Siemens PLM STAR-CCM+ Homepage. Available online: https://mdx.plm.automation.siemens.com/star-ccm-plus (accessed on 14 March 2019).

32. Blender Org. Manual Homepage. Available online: https://docs.blender.org/manual/de/dev/physics/rigid_body/introduction.html (accessed on 14 March 2019).

33. MatWeb Material Property Data. Available online: http://www.matweb.com/search/DataSheet.aspx?MatGUID=c8c56ad547ae4cfabad15977bfb537f1 (accessed on 14 March 2019).

34. MatWeb Material Property Data. Available online: http://www.matweb.com/search/DataSheet.aspx?MatGUID=cbe7a469897a47eda563816c86a73520 (accessed on 21 March 2019).

35. Di Renzo, A. and Di Maio, F. P. Comparison of contact-force models for the simulation of collisions in DEM-based granular flow codes. *Chemical Engineering Science* **2004**. *59*, 525–541. DOI=10.1016/j.ces.2003.09.037.

36. Zhu, H. P., Zhou, Z. Y., Yang, R. Y., and Yu, A. B. Discrete particle simulation of particulate systems: Theoretical developments. *Chemical Engineering Science* **2007**. *62*, 3378–3396. DOI=10.1016/j.ces.2006.12.089.

37. Eppinger, T., Jurtz, N., and Aglave, R. Automated workflof for spatially resolved packed bed reactors with spherical and non-spherical particles, 10th International Conference on CFD in Oil & Gas, Metallurgical and process Industries SINTEF, Trondheim, Norway, 17-19th June 2014.

38. Wehinger, G. D., Eppinger, T., and Kraume, M. Evaluating Catalytic Fixed-Bed Reactors for Dry Reforming of Methane with Detailed CFD. *Chemie Ingenieur Technik* **2015**. *87*, 734–745. DOI=10.1002/cite.201400153.

39. Youtube. Available online: https://www.youtube.com/watch?v=Zz3I5Gbrguw (accessed on 7 April 2019).

40. Blender Org. Manual Homepage. Available online: https://docs.blender.org/manual/de/dev/physics/rigid_body/properties.html (accessed on 11 July 2018).

41. Dhole, S. D., Chhabra, R. P., and Eswaran, V. A numerical study on the forced convection heat transfer from an isothermal and isoflux sphere in the steady symmetric flow regime. *International Journal of Heat and Mass Transfer* **2006**. *49*, 984–994. DOI=10.1016/j.ijheatmasstransfer.2005.09.010.

42. Eppinger, T., Seidler, K., and Kraume, M. DEM-CFD simulations of fixed bed reactors with small tube to particle diameter ratios. *Chemical Engineering Journal* **2011**. *166*, 324–331. DOI=10.1016/j.cej.2010.10.053.

43. Dixon, A. G. Correlations for wall and particle shape effects on fixed bed bulk voidage. *Can. J. Chem. Eng.* **1988**. *66*, 705–708. DOI=10.1002/cjce.5450660501.

44. Wehinger, G. D., Fütterer, C., and Kraume, M. Contact Modifications for CFD Simulations of Fixed-Bed Reactors: Cylindrical Particles. *Ind. Eng. Chem. Res.* **2017**. *56*, 87–99. DOI=10.1021/acs.iecr.6b03596.